Journal of Nuclear Materials 540 (2020) 152392

Contents lists available at ScienceDirect

Journal of Nuclear Materials

journal homepage: www.elsevier.com/locate/jnucmat

In-situ studies on the mechanical properties of He ion irradiated nanotwinned Ag

T. Niu [a], Jin Li [b, **], Y. Zhang [a], J. Cho [a], Jie Ding [a], R. Su [a], S. Xue [a], C. Fan [a], Z. Shang [a], Di Chen [c, d], Y. Wang [d], H. Wang [a, e], X. Zhang [a, *]

[a] School of Materials Engineering, Purdue University, West Lafayette, IN, 47907, USA
[b] Institute of Special Environments Physical Sciences, Harbin Institute of Technology, Shenzhen, 518055, China
[c] Department of Physics, University of Houston, Houston, TX, 77204, USA
[d] Materials Science and Technology Division, Los Alamos National Laboratory, Los Alamos, NM, 87545, USA
[e] School of Electrical and Computer Engineering, West Lafayette, IN, 47907, USA

ARTICLE INFO

Article history:
Received 20 January 2020
Received in revised form
4 July 2020
Accepted 8 July 2020
Available online 18 July 2020

ABSTRACT

Recent studies show that twin boundaries are effective defect sinks in eliminating radiation-induced defects. However, the influence of radiation-induced defects on the mechanical behavior of nanotwinned (NT) materials is less well understood. In this study, we investigate the mechanical properties of He ion irradiated NT Ag. *In-situ* micropillar compression tests show that deformation induces prominent detwinning in as-deposited NT Ag, whereas He ion irradiation alleviates detwinning during deformation of NT Ag. The radiation hardening mechanism and the influence of He bubbles on the deformation behavior of NT Ag are discussed.

1. Introduction

High-energy particle irradiations induce a considerable amount of point defects, which migrate and interact with each other, forming dislocation loops [1], stacking fault tetrahedrons (SFTs) [2] and cavities [3,4]. These defect clusters act as barriers for dislocation movement and increase the stress necessary to initiate plastic deformation of irradiated materials, resulting in irradiation hardening [5,6]. Other detrimental effects, such as void swelling and He embrittlement, limit the operation conditions and service reliability of nuclear reactor materials [7,8]. Great efforts have been made to design radiation tolerant materials. Recent studies show that interfaces, such as grain boundaries (GBs) [9–12], phase boundaries [13–17] and twin boundaries (TBs) [18–22], can act as defect sinks and promote the recombination and annihilation of irradiation-induced defects, thus alleviating irradiation damage [23,24]. For example, nanocrystalline (nc) metals are found to greatly reduce defect density and curtail radiation hardening compared to their bulk counterparts after radiation [11,12,25–29]. Both experiments and simulation studies reveal the role of grain boundaries in trapping and removing defects [10,12]. Size-dependent reduction of He bubble density and irradiation hardening have been reported for a variety of multilayer systems, where smaller layer thickness leads to less hardening after irradiation [14–17,30,31].

Nanotwinned (NT) metals have drawn intense interest for the past decade due to their high strength, high fracture toughness and good ductility [32–37]. Despite their attractive mechanical properties, it is often anticipated that TBs are not effective defect sinks for irradiation damage due to their low energy configuration [38,39]. However, several recent studies have shown the ability of TBs in eliminating radiation induced defects [18–22]. MD simulations reported the deconstruction of SFTs during their interactions with coherent twin boundaries (CTBs) [40], and the MD prediction was then validated via *in-situ* Kr ion irradiation experiment on NT Ag [18]. TB affected zones were also observed, where time accumulative defect density was prominently reduced near TBs [20]. It has also been reported that TBs can change their geometry during irradiation to accommodate the distortion caused by dislocation loops and “self-heal” after capturing defects [22]. The irradiation resistance of NT metals can be further enhanced by combining nanotwins with other nanostructures [21]. Chen et al. showed that the introduction of nanovoids in conjunction with nanotwins (NTs)

* Corresponding author.
** Corresponding author.
E-mail addresses: lijin2019@hit.edu.cn (J. Li), xzhang98@purdue.edu (X. Zhang).

https://doi.org/10.1016/j.jnucmat.2020.152392
0022-3115/

greatly enhanced the radiation tolerance of Cu, and TBs were found to provide fast diffusion channels to transport defects and accelerate defects elimination by nanovoids [21].

Similar to GB migration, the frequent migration of TBs and twin thickness dependent detwinning were observed under both *in-situ* nanoindentation and *in-situ* Kr ion irradiation [41–45]. Simulation studies showed that incoherent twin boundaries (ITBs) are composed of arrays of Shockley partials [43,46], and the migration of ITBs is achieved by collective glide of Shockley partials, thereby causing detwinning [43]. It has also been reported that, under Kr ion irradiation, Frank partials climb due to defect-TB interaction and defect absorption could be an alternative mechanism to advance or retreat ITBs [42]. A recent MD simulation study investigated the interactions between nanovoids and migrating GBs. Their results suggest that the pinning strength of voids on GBs is highly dependent on the surface area of voids, the GB energy and the contact angle between voids and GBs [47]. However, the influence of He bubble size, pressure and He-to-vacancy ratio on the pinning effect of bubbles on ITBs is less well understood due to the limited studies on ITB-bubble interactions.

Although significant efforts have been made in studying the microstructure evolution of NT metals subjected to irradiations, the irradiation effect on the mechanical behaviors of NT metals remains less well understood. In this study, we investigate the influence of He implantation on the mechanical properties of NT Ag by *in-situ* micropillar compression tests in a scanning electron microscope. Deformation behaviors of NT Ag before and after irradiation were compared, and factors contributed to irradiation hardening were discussed.

2. Experimental

Epitaxial Ag thin film with a total thickness of 1 μm was deposited on HF etched Si (111) substrate by DC magnetron sputtering at room temperature. The base pressure of the vacuum chamber was evacuated to below 5×10^{-8} torr before deposition. He ion irradiation experiments were subsequently performed at Ion Beam Materials Laboratory at Los Alamos National Laboratory. The stopping and range of ions in matter (SRIM) simulation was performed by using the with Kinch-Pease method to estimate the radiation damage in unit of displacements-per-atom (dpa) and calculate depth profile of He concentration. Three sets of He irradiation at energies of 50, 100 and 200 keV with respective ion dose of 1.06, 2.05 and 3.99×10^{16} ions/cm^2 were performed sequentially at room temperature to produce a uniform irradiation region, reaching an average dose level of ~1 dpa. In addition, another series of He implantation with the same ion energies doses performed to irradiate the NT Ag to 5 dpa. The corresponding doses were 5.30×10^{16} ions/cm^2 at 50 keV, 10.25×10^{16} ions/cm^2 at 100 keV, and 20.00×10^{16} ions/cm^2 at 200 keV. X-ray diffraction experiments were performed on a Panalytical Empyrean system (Cu Kα radiation) at room temperature. Cross-sectional transmission electron microscopy (XTEM) samples were mechanically grinded and polished, followed by dimpling and low energy Ar ion milling by a Gatan PIPS II system. TEM experiments were performed on a Thermo Fischer Scientific/FEI Talos 200X microscope with Super-X EDS detectors operated at 200 kV. Micropillars of as-deposited and irradiated NT Ag with ~500 nm in diameter and a diameter-to-height ratio of 1:2 were fabricated by focused ion beam (FIB) using the FEI Quanta 3D FEG scanning electron microscope (SEM). *In-situ* pillar compression tests were performed using a Hysitron PI 88 × R PicoIndenter equipped with a 5 μm diamond flat punch inside an FEI quanta 3D FEG SEM microscope. A piezoelectric actuator on the capacitive transducer enables the force-displacement data collection, and the morphology evolution of pillars was captured concurrently during deformation. The average drift rate of 0.2–0.7 nm/s was estimated and compensated in preloading process for 45 s, and the estimated force measurement noise is ±8 μN. The applied strain rate is maintained at 5×10^{-3} s^{-1}. The deformed pillars were thinned by FIB for post-compression TEM analysis.

3. Results

XTEM image of the as-deposited film taken from [$01\bar{1}$] zone axis (Fig. 1(a)) shows a high density of nanotwins. The histogram in Fig. 1(b) shows the average twin spacing of as-deposited NT Ag film is 9 nm. In comparison, CG Ag has large grain with an average grain size of ~60 μm. X-ray diffraction (XRD) pattern in Fig. S1 shows that the as-deposited Ag film has strong (111) texture. After irradiation, the Ag (111) peak position is slightly shifted to lower angle by 0.12°. As shown in Fig. 2, the SRIM simulation implies that the He concentration reaches a plateau of ~2.0 at% at the depth of 200–500 nm after sequential radiation. The average damage level is ~1.1 dpa.

Under-focus XTEM images in Fig. 3 are captured at different depth to study the He bubble density evolution along projected ion path. For CG and NT Ag after 1 dpa irradiation, the bubble size shows very little variation along the penetration depth as shown in Fig. 3(a and b). The thickness of TEM foils shown in Fig. 3 was estimated using convergent beam electron diffraction (CBED) method to calculate the bubble density [48]. These TEM foils are usually tapered and the foil thickness gradually increase with the increasing distance from the foil tip as shown in Fig. S2a. The thickness at the surface edge of foils typically ranges from 60 to 70 nm, while the average foil thickness is around 110–120 nm. Fig. S2 shows an example of foil thickness measurement of NT Ag irradiated to 1 dpa. The depth profile of He bubble density in Fig. 4(a) reveals that the general trend of bubble density variation matches well with He concentration profile. The bubble density in CG Ag irradiated to 1 dpa increases to a plateau at 200–600 nm from surface as shown in Fig. 4(a). In comparison, the maximum bubble density in NT Ag is reached at ~300 nm. The total bubble induced swelling ($\Delta V/V$) in NT Ag after 1 dpa irradiation is ~0.13%, in comparison with ~0.45% for CG Ag irradiated to the same dose level as tabulated in Table 1. Irradiation to 5 dpa produced a mixture of small spherical bubbles and large faceted bubbles in NT Ag. As shown in Fig. 3(c_1), the majority of bubbles within 100 nm from surface are spherical with a typical size of ~1 nm, while faceted bubbles were occasionally observed. Beyond 300 nm, faceted bubbles become the dominant type of defects as shown in Fig. 3(c_2-c_4) and Fig. 4(b). The depth profile of average bubble size in NT Ag irradiated to 5 dpa is shown in Fig. S5. The total swelling is estimated to be ~0.66%, which is almost 5 times of that of NT Ag irradiated to 1 dpa. In all three systems, at ~750 nm where He concentration drops dramatically to nearly zero, He bubbles diminished abruptly. High resolution TEM (HRTEM) image taken from NT Ag after 1 dpa irradiation provides more details of microstructure change after irradiation. As shown in Fig. S3(a), while some bubbles are located along CTBs and ITBs, in general, there is no preference for bubbles to aggregate along CTBs. Meanwhile, as a result of the interactions between TBs and irradiation-induced defects, we observed abundant stacking faults (SFs) decorating along CTBs (Fig. S3b).

Fig. 5 compares the microstructure evolution of NT Ag after irradiation to 1 dpa and 5 dpa. The average twin spacing increases slightly from 9 to 11 nm after 1 dpa irradiation and to 12 nm when irradiated to 5 dpa as shown in Fig. 5(a and b). The statistics of grain size distribution in Fig. 5(c_2) and (d_2) reveals little grain size difference. Furthermore, rel-rod dark field TEM images reveal the formation of Frank loops in both scenarios as shown in Fig. 5(e and f).

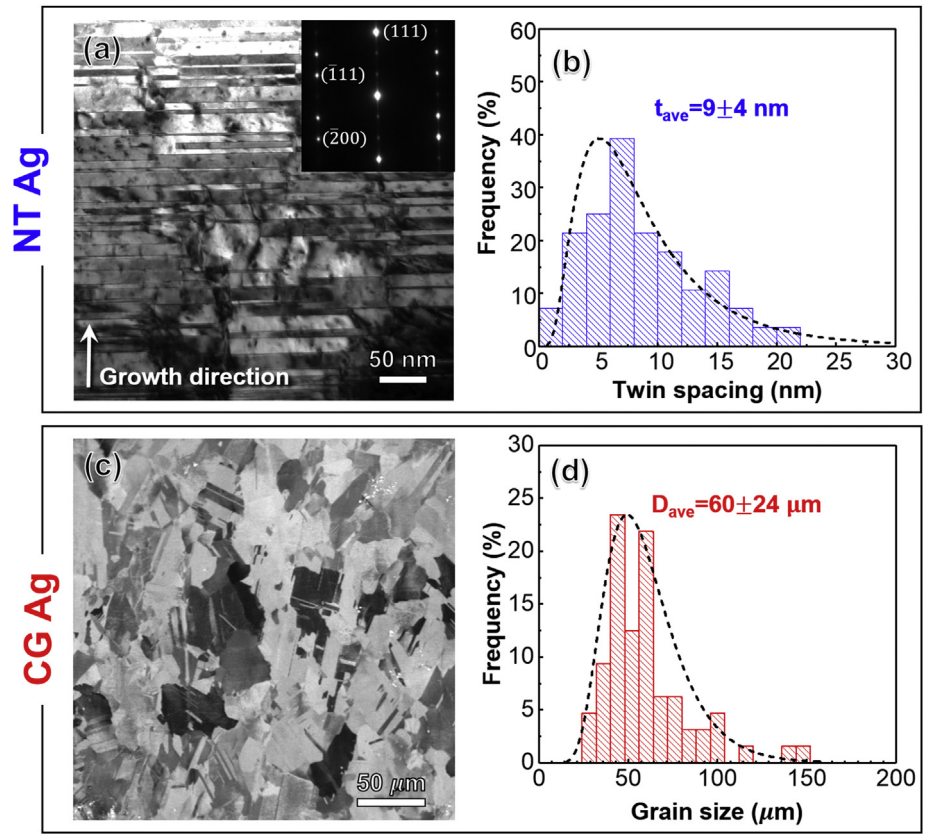

Fig. 1. (a) Cross-section TEM (XTEM) image of as-deposited NT Ag from <110> zone axis showing a high density of growth twins. (b) Statistics showing the as-deposited NT Ag film has an average twin thickness of 9 nm. (c) SEM image of CG Ag acquired using ion channeling contrast. (d) The grain size distribution of CG Ag. The average grain size is 60 μm.

In-situ micropillar compression tests were conducted to study the deformation mechanism and irradiation hardening behavior in CG Ag and NT Ag before and after irradiation. Shown in Fig. 6 are the engineering stress-strain curves and corresponding SEM snapshots revealing the pillar morphology evolution during compression tests of CG Ag. Multiple engineering stress-strain curves are presented in Fig. 6 and Fig. 7 to ensure the reproducibility of the results. Before irradiation, deformation was mostly localized on pillar top and several shear bands formed near pillar top when compressed to a strain level of 15% as shown in Fig. 6a_2-a_4. The flow stress of CG Ag is ~125 MPa (Fig. 6a_1). In comparison, the irradiated CG Ag pillar deformed in a different manner where the pillar top (irradiated portion) experienced much less deformation than the rest of the pillar, and shear bands initiated from the middle of the pillar instead of the top. After irradiation to 1 dpa, the flow stress nearly doubled in CG Ag (Fig. 6b_1). See Supplementary Videos 1 and 2 for more details.

Supplementary video related to this article can be found at https://doi.org/10.1016/j.jnucmat.2020.152392

The deformation behavior of NT Ag before and after irradiation to 1 and 5 dpa during in-situ micropillar compression tests is summarized in Fig. 7. The as-deposited pillar deformed uniformly up to 5% of strain (Fig. 7a_2-a_3). By 10% of strain, both the pillar top and base experienced prominent dilations as shown in the SEM snapshots in Fig. 7(a_2-a_5). In contrast, the pillars of NT Ag irradiated to 1 and 5 dpa deformed uniformly by 5% of strain; and by 15% of strain, the pillars tops underwent much less dilation, whereas the bottom half (the mostly unirradiated region) expanded during deformation beyond 5% of strain. The engineering stress-strain curves of three types of pillars are shown in Fig. 7a_1-c_1. See Supplementary Videos 3–5 for more details.

Supplementary video related to this article can be found at https://doi.org/10.1016/j.jnucmat.2020.152392

Due to the non-uniform deformation occurred during pillar compression, in-plane stress-strain curves shown in Fig. 8 were calculated using the instantaneous pillar top diameter measured from in-situ snapshots to compare the strength difference before and after irradiation. The in-plane strain were calculated as:

$$\varepsilon_{in-plane} = \ln(A_i / A_0) = \ln\left(r_i^2 \Big/ r_0^2\right) \quad (1)$$

where A_i is the instantaneous cross section area of the pillars, A_0 is original cross section area, r_i is the instantaneous pillar diameter and r_0 is the original pillar diameter. The measurement of instantaneous diameter was performed at pillar top as shown in Fig. S7. As shown in Fig. 8 (a) and (b), the in-plane strain for the pillar in CG Ag and NT Ag before irradiation is higher than 30%, implying highly localized deformation on pillar top. Taking the flow stress from 5% in-plane strain, irradiation to 1 dpa induced ~170 MPa stress increment in CG Ag. For NT Ag, the as-deposited pillar has a flow stress of ~827 MPa. Interestingly, we found the stress increment after irradiation to 1 dpa is ~290 MPa, greater than the strengthening after 5 dpa irradiation, ~215 MPa.

Further examinations of the microstructures of the deformed pillars were conducted by TEM experiments. Fig. 9(a) shows the overview of deformed (to a strain of 10%) pillar of the as-deposited NT Ag. The bright contrast comes from the crystal rotation and the loss of TBs during compression. As shown in Fig. 9(b–d), the evolution of selected area diffraction (SAD) pattern across different depth further reveals the twin density variations and the diminution of ITBs. The detwinning band has a width varying from 163 to

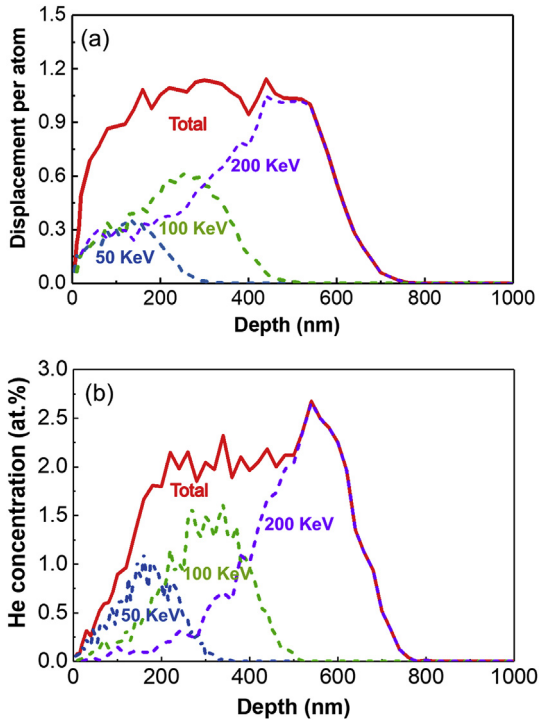

Fig. 2. The depth profile of (a) radiation damage in the unit of dpa and (b) He concentration, obtained from the SRIM simulations of Ag subjected to sequential He ion irradiation at 50 keV, 100 keV and 200 keV. The three sequential irradiations to corresponding dose of 1.06×10^{16} ions/cm^2, 2.05×10^{16} ions/cm^2, and 3.99×10^{16} ions/cm^2 lead to plateaus of displacement damage at ~1 dpa, and 2 at.% He concentration.

255 nm near the pillar top. In comparison, the detwinning region near the base is a bit irregular, located in the center of the deformed pillar. Fig. 9(e) from the detwinning region shows diffuse and tapered ITBs, where detwinning is accomplished by collective glide of arrays of Shockley partials. HRTEM image in Fig. 9(f) shows the generation of thick SF ribbons adjacent to CTBs and several dislocation debris on the inclined {111} slip planes due to dislocation-TB interactions.

The microstructure of the deformed NT Ag irradiated to 1 dpa is shown in Fig. 10. The overview in Fig. 10(a) shows the detwinning region near the pillar top has a band with width varying from 73 to 113 nm, much narrower than that in the deformed as-deposited pillar. The detwinning region near the pillar base also has irregular geometry with a maximum width of 187 nm. The SAD patterns taken from the top and middle part of the pillar as shown in Fig. 10(b and c) exhibit typical twin patterns, while the twin spots diminished in the SAD pattern taken near the pillar base (Fig. 10(d)). TEM image in Fig. 10(e) shows the retention of 9R phase, where the ITB remains sharp rather than diffuse as observed in as-deposited NT Ag pillar in Fig. 9(e). Fig. 10(f) shows a typical CTB with numerous steps after deformation. These steps are known as the twinning dislocations, resulting from the transmission of mixed dislocation across CTBs. For the NT Ag irradiated to 5 dpa, the deformation is mainly localized near pillar base as shown in Fig. 11 (a). The detwinning region near pillar top has a maximum width of 68 nm, in comparison to the 188 nm bandwidth near the pillar base. The SAD pattern in Fig. 11(b) reveals a crystal rotation of ~9° after deformation near the pillar top. The HRTEM in Fig. 11(e) shows the interactions between ITBs and faceted He bubbles, where part of the ITBs were pinned by the bubbles.

4. Discussion

4.1. Irradiation induced He bubbles and microstructure evolution

Helium often has extremely low solubility in metals and can combine with vacancies generated during irradiation to form He bubbles [49,50]. Fig. 4 (a) shows the depth profile of He bubble density and the simulated He concentration at a damage level of 1 dpa. He ion implantation at multiple energies and doses results in a bubble density plateau of ~2.15×10^{24} m^{-3} at the depth of 200−500 nm in CG Ag and ~1.75×10^{24} m^{-3} at the depth of 300−500 nm in NT Ag. It is worth mentioning that the bubble density estimation can be affected by a variety of factors, including the existence of bubbles below the TEM resolution limits, the foil thickness measurement error as well as the bubble overlap effect. The average spacing (l) between bubbles observed in irradiated Ag can be estimated as [5,51]:

$$l = \sqrt{N_B \cdot d_B} \tag{2}$$

where N_B is the bubble density, and d_B is the average bubble size. The average spacing was calculated to be 20−30 nm. The bubble overlap may be inevitable given the high bubble density and small spacing, and may result in the underestimation of bubble density.

Irradiation to 5 dpa leads to the formation of large faceted bubbles as displayed in Fig. 3(c). These faceted bubbles form in regions irradiated with higher He ion energies. During radiation, the gradual build-up of He concentration is accompanied by the diffusion and accumulation of He into the bubbles, leading to the increase of bubble pressure [8,49]. The raising pressure then promotes the bubble growth by absorbing vacancies to release the internal pressure. These vacancies necessary for the growth of bubbles must be created by those unclustered vacancies created in the cascades. Irradiation with light ions like He generate predominately isolated Frenkel pairs due to the relatively low recoil atom energies [52]. Previous studies show that the increment of irradiating particle energy and thus the primary knock-on atom energy can result in either the increase of displacement cascade size or larger number of subcascades [53]. Despite the higher probability of in-cascade recombination, the defect density within the cascades was found to increase with increasing particle energy [53]. Hereby, it is expected that increasing the He ion energy will lead to the generation of more unclustered vacancies. Furthermore, as shown in Fig. 2, the He concentration is also much higher for regions with higher ion energies.

It has been suggested that excessive gas atoms compel the overpressurized bubbles to become faceted so as to reduce the total system energy [54,55]. The model proposed by Goodhew considers the total free energy change and the bubble shape evolution after introducing more gas atoms, and the influence of bubble shape (defined by $s\gamma$) on total free energy (E_T) can be expressed as [55]:

$$\frac{d(E_T)}{d(s\gamma)} = V_0\left[\frac{6}{a} + \frac{4}{aK}\left(P - \frac{4s\gamma}{a}\right)\right] \tag{3}$$

where s is the shape parameter ($s < 1$ for a sphere, $s = 1$ for a cube, and $s > 1$ for a less regular shape), γ is the surface energy, V_0 is the bubble volume, a is the side length of a cubic bubble, P is the bubble pressure and K is the bulk modulus. $\frac{d(E_T)}{d(s\gamma)}$ is always positive for equilibrium and overpressurized bubbles ($P \geq \frac{4s\gamma}{a}$). Hence, the reduction of E_T requires a decrease in $s\gamma$ value. This observation indicates that the bubbles tend to facet on low energy planes [55]. The faceted bubble formation in high He concentration region was

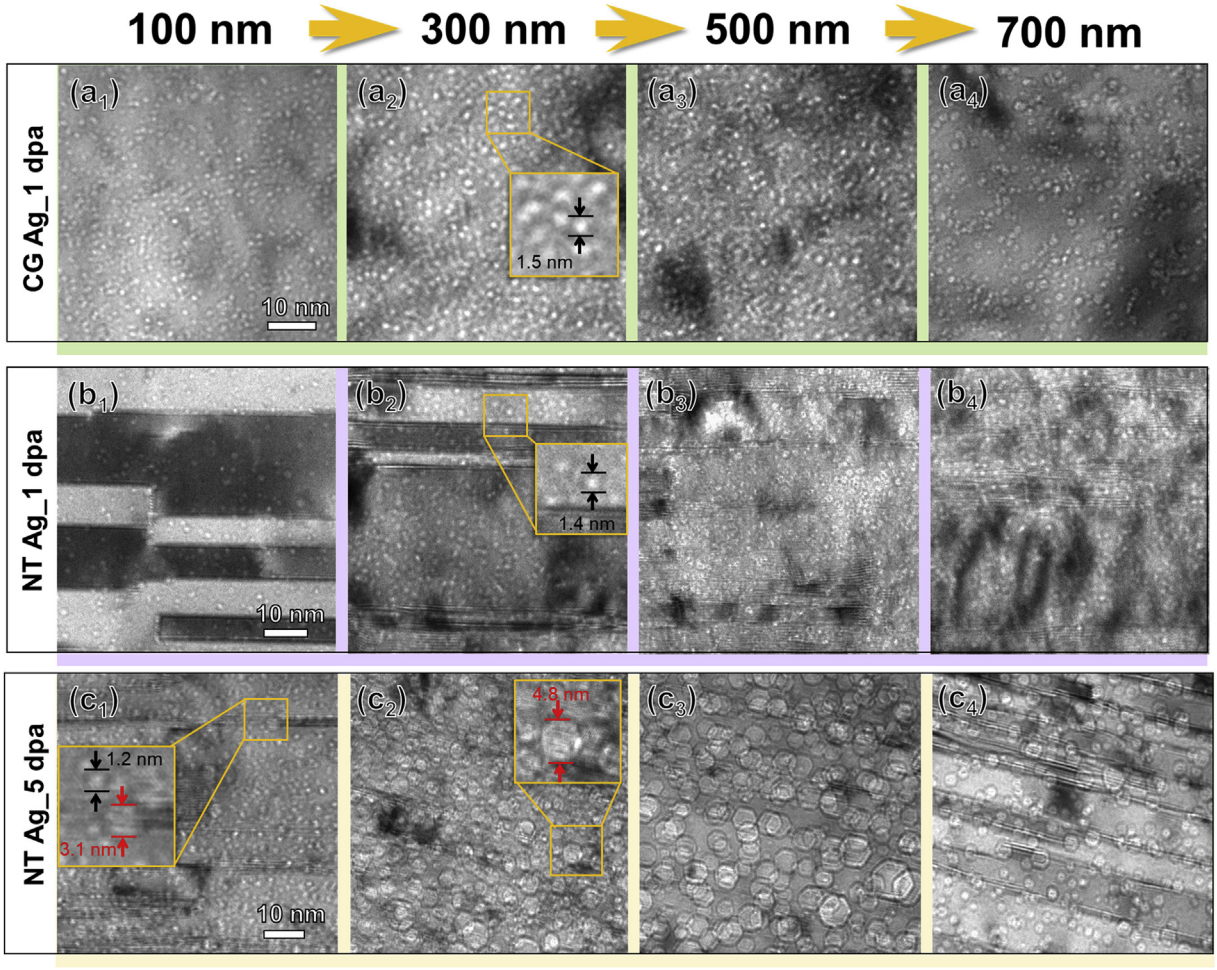

Fig. 3. TEM micrographs at different penetration depth of (a) CG Ag and (b) NT Ag after 1 dpa irradiation and (c) NT Ag irradiated to 5 dpa. The inset shows typical bubble size in the three systems. (c_1-c_4) were taken out of <110> zone axis so as to improve the contrast for imaging bubbles.

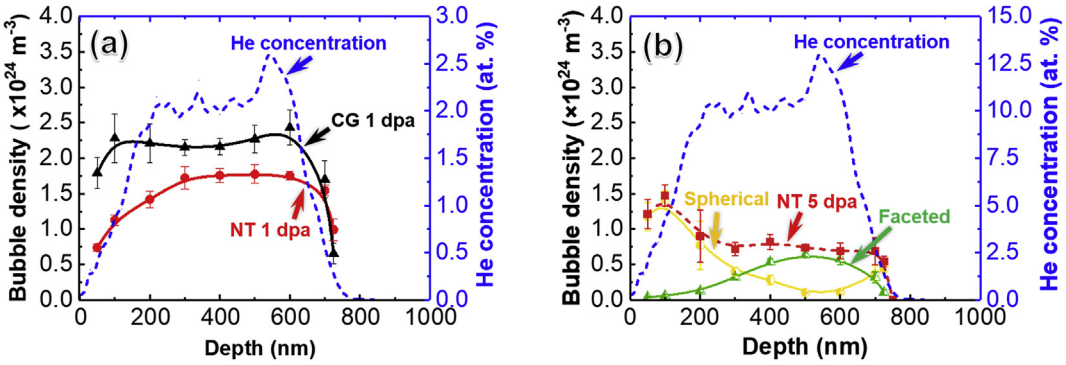

Fig. 4. (a) Depth dependent He bubble density distribution in CG Ag and NT Ag after irradiation to 1 dpa correlates to the He concentration profile. (b) The depth profile of bubble density in NT Ag irradiated to 5 dpa. The majority of bubbles within 300 nm from surface are small spherical bubbles (yellow solid line) while large faceted bubbles dominate thereafter (green solid line). The total bubble density is shown as the red dash line. (For interpretation of the references to colour in this figure legend, the reader is referred to the Web version of this article.)

previously observed in He ion irradiated V/Ag multilayers [56]. Therefore, the formation of large faceted bubbles may be favored by the larger quantity of unclustered vacancies and higher He concentration.

It has been reported that dislocations, GBs and phase boundaries are favorable sites for He bubble nucleation due to their capacity in trapping He atoms [50]. In NT Ag, there is no obvious segregation of He bubbles along CTBs due to the high coherency of CTBs. In comparison, ITBs provide more excess free volume for He atoms to reside and consequently, bubbles tend to decorate along ITBs as shown in Fig. S3(a). In addition, the generation of thick SF ribbons adjacent to CTBs is observed after irradiation as shown in Fig. S3(b), which may originate from the interactions between dislocation loops and CTBs or the destruction of SFTs by CTBs [18]. Interactions

Table 1
Comparison of bubble pressure, He molar volume, He-to-vacancy ratio and concentration of He atoms stored in bubbles between CG Ag and NT Ag.

		Pressure (GPa)	He molar volume (cm^3/mol)	He-to-vacancy ratio	He concentration in bubbles (at%)	Swelling (%)
CG Ag_1 dpa		3.1	6.05	1.7	0.71	0.45
NT Ag_1 dpa		4.2	6.68	1.5	0.27	0.13
NT Ag	Spherical	3.3	6.53	1.6	0.14	0.66
5 dpa	Faceted	1.3	9.08	1.1	0.65	

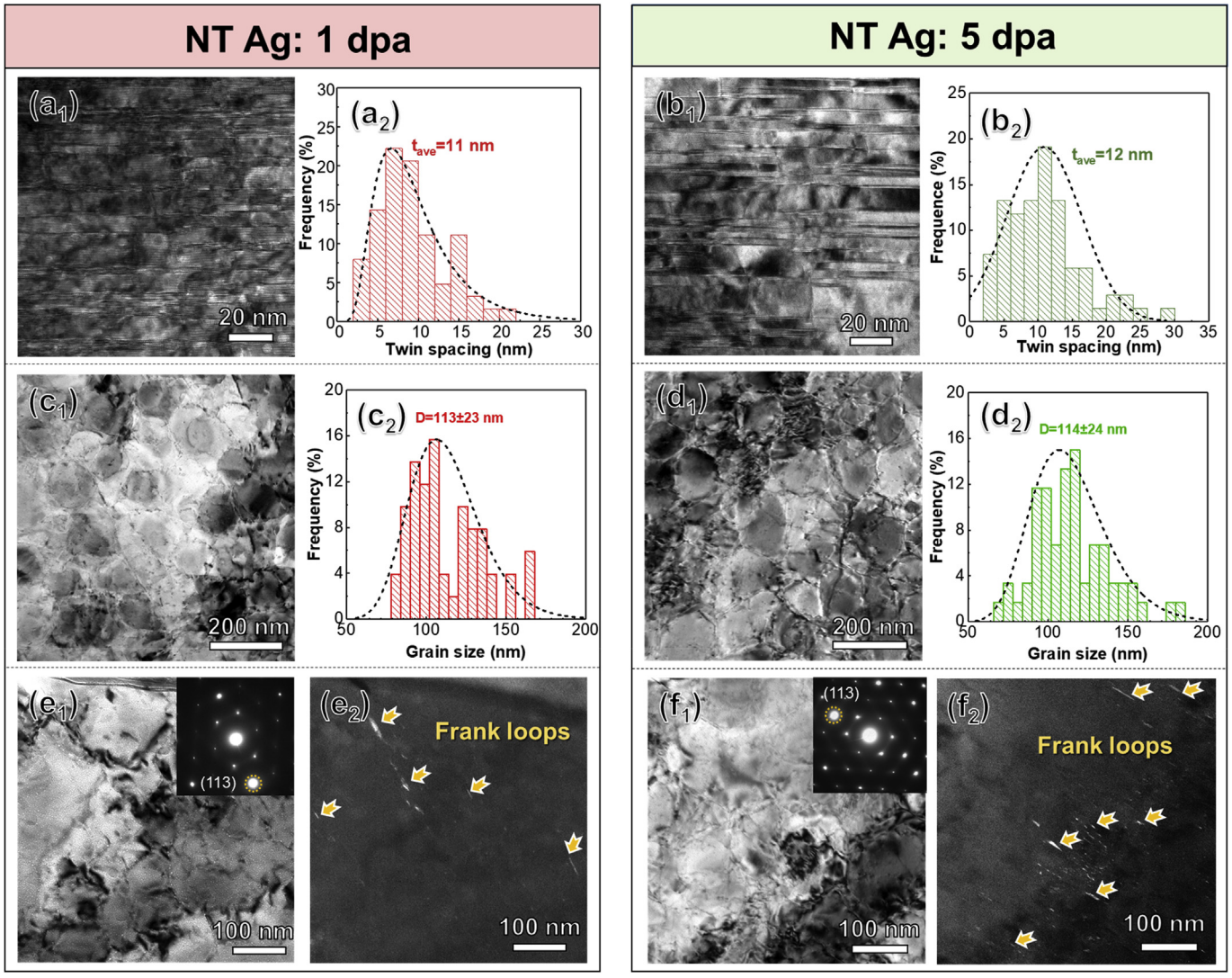

Fig. 5. Comparison of the microstructure evolution of NT Ag after irradiation to 1 dpa and 5 dpa. (a–b) XTEM micrographs and corresponding statistics showing slight twin spacing increase after irradiation to 1 dpa and 5 dpa. (c–d) Negligible grain coarsening in NT Ag after irradiation to 1 dpa and 5 dpa as shown in TEM images and grain size statistical distribution. (e–f) Rel-rod images showing the Frank loop distribution in NT Ag irradiated to 1 dpa and 5 dpa.

between ITBs and dislocation loops during irradiation often lead to TB migration and subsequent detwinning [42,44]. As shown in Fig. 5 the twin spacing increases slightly from 9 to 11 nm after irradiation to 1dpa, and to 12 nm after irradiation to 5 dpa, and no obvious grain coarsening is observed.

We now attempt to estimate the pressure built-up inside He bubbles. The equilibrium bubble pressure can be estimated by [57]:

$$P = 2\gamma/R \quad (4)$$

where P is the bubble pressure, γ is the surface energy, and R is the radius of bubble. For NT Ag irradiated to 1 dpa, the average bubble diameter is 1.2 nm. Given that $\gamma_{Ag} = 1.25\,J/m^2$ [58], the bubble pressure is estimated to be 4.2 GPa. This value constitutes the lower bound estimation since He bubbles could be over pressurized. Previous studies suggested that the pinning effect of He bubbles on dislocation migrations is tightly associated with He-to-vacancy ratio. By using Mills' equation of state (EOS) for high pressure He bubbles, we estimate the molar volume of He to be 6.05 cm^3/mol. Since the atomic density of Ag (ρ) is 58.6/nm^3, we derive the average number of vacancies in each bubble is 53 and 90 He/bubble for Ag, corresponding to 1.7 He/vacancy. The concentration of He

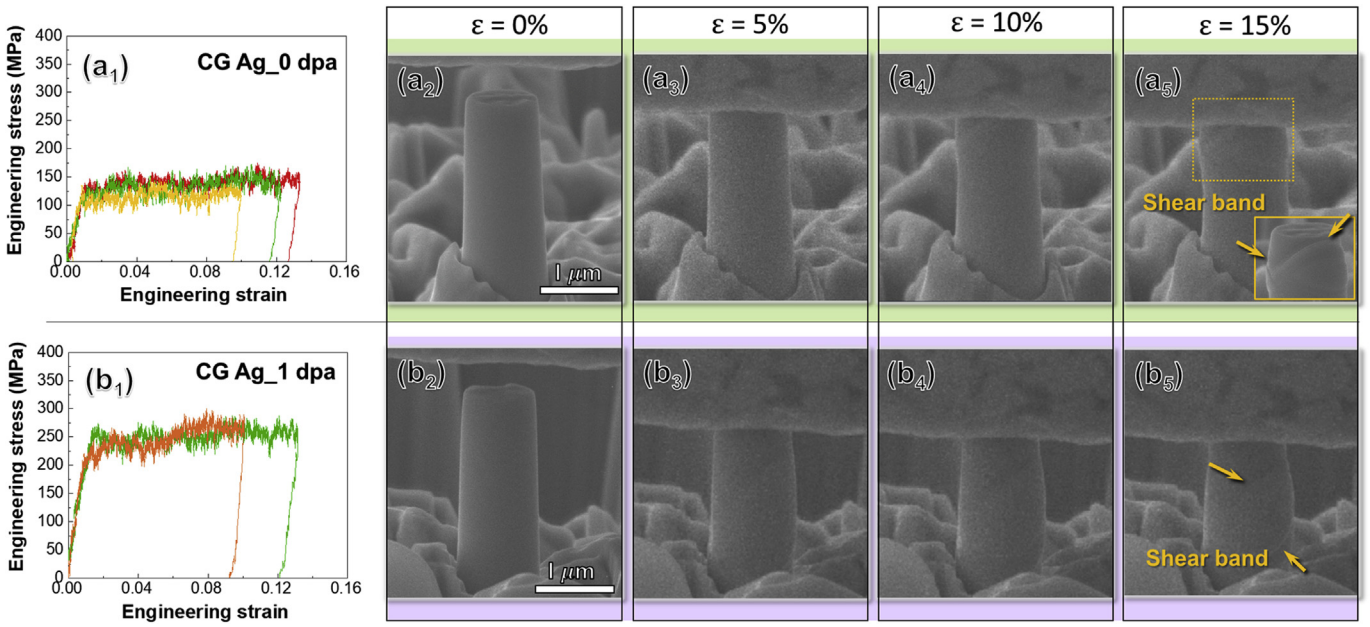

Fig. 6. In-situ micropillar compression tests on CG Ag before and after irradiation. (a_1) Engineering stress-strain curves for pristine CG Ag and (a_2-a_5) in-situ pillar compression snapshots showing dilation near pillar top and formation of shear bands. (b_1) Representative engineering stress-strain curves of irradiated CG Ag shows obvious stress increment. (b_2-b_5) In-situ pillar compression snapshots of irradiated CG Ag showing Localized deformation with shear band formation in the middle of pillar. See Supplementary Videos 1 and 2 for more details.

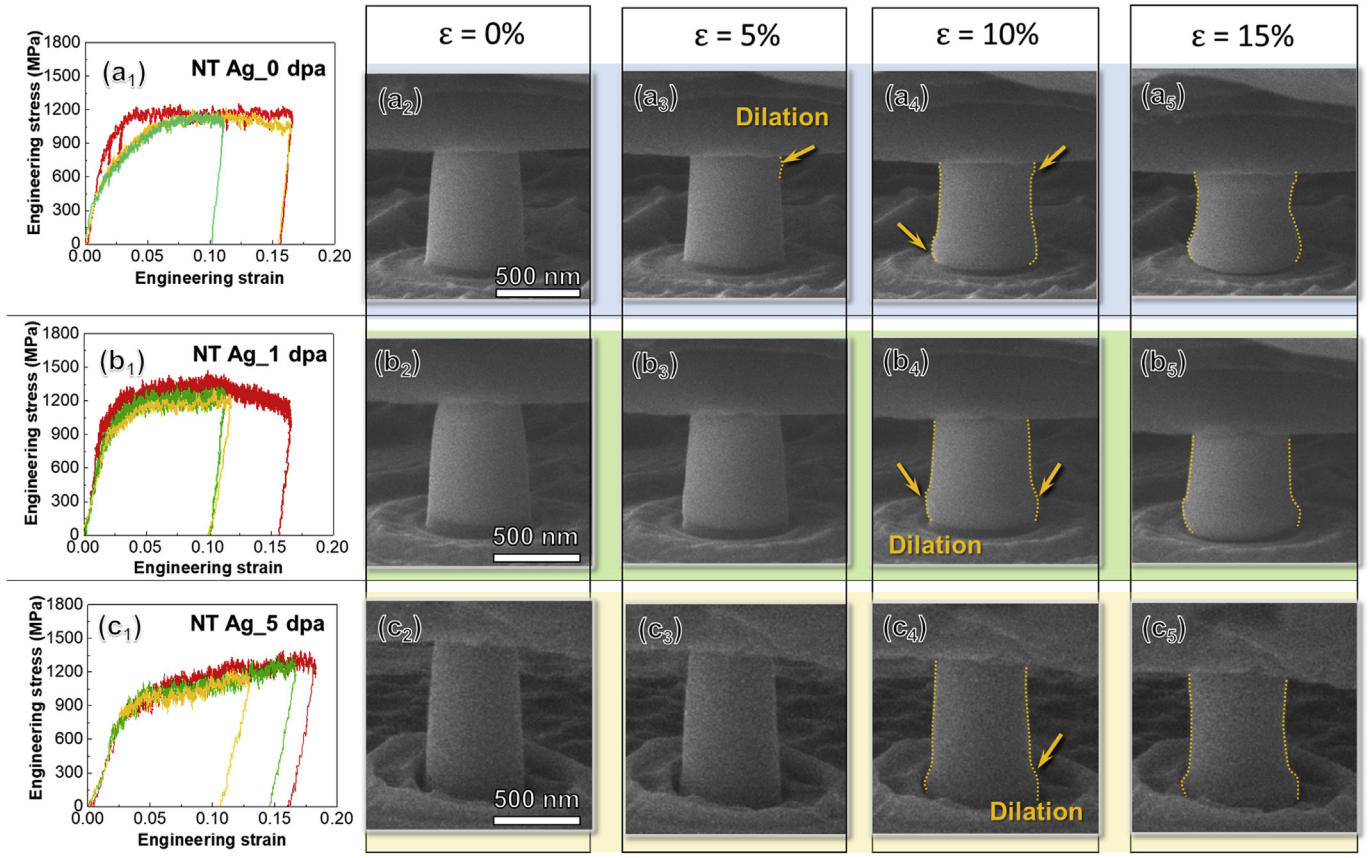

Fig. 7. In-situ micropillar compression tests on NT Ag before and after irradiation. (a_1) Engineering stress-strain curves for as-deposited NT Ag. (a_2 -a_5) In-situ pillar compression snapshots of as-deposited NT Ag showing dilation near both pillar top and bottom. (b_1) Engineering stress-strain curves of NT Ag irradiated to 1 dpa show obvious stress increment (~250 MPa). (b_2 -b_5) In-situ compression snapshots of NT Ag irradiated to 1 dpa reveal that deformation was mainly accommodated by the bottom part (unirradiated region) of the pillar. (c_1) Engineering stress-strain curves of NT Ag irradiated to 5 dpa. (c_2 -c_5) In-situ compression snapshots shows that yielding happened first in unirradiated region (pillar base) in NT Ag irradiated to 5 dpa. See Supplementary Videos 3-5 for more details.

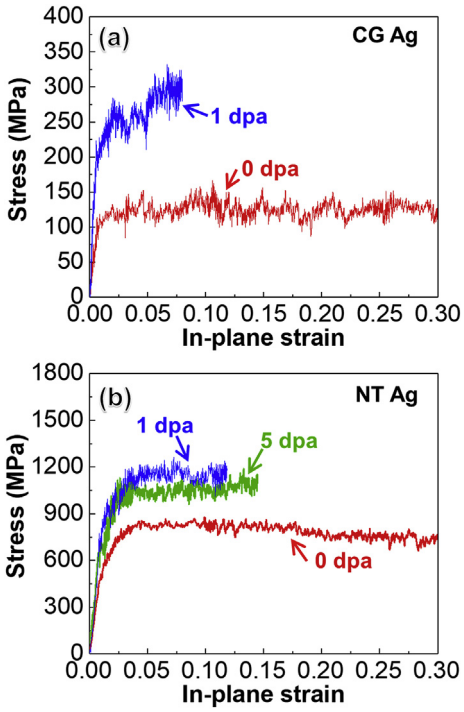

Fig. 8. In-plane stress-strain curve of (a) CG Ag and (b) NT Ag before and after irradiation. The in-plane strain was calculated based on the instantaneous pillar diameter near pillar top measured from in-situ pillar compression snapshots, i.e. $\varepsilon_{in-plane} = (A_i/A_0) = (r_i^2/r_0^2)$. Irradiation hardening was observed for both CG and NT Ag.

atoms stored in bubbles is estimated to be 0.27 at%, in comparison to the SRIM simulated average He concentration of 2.0 at%. For CG Ag irradiated to 1 dpa, the calculation yields a He molar volume of 6.68 cm^3/mol and a He-to-vacancy ratio of 1.5. The estimated He concentration stored in He bubbles in CG Ag irradiated to 1 dpa is 0.71 at%. The discrepancy between calculated He concentration and the SRIM result indicates that a certain amount of He atoms may reside near TBs and submicroscopic defects, e.g. He-vacancy clusters below the resolution limit of TEM. The results for NT Ag irradiated to 5 dpa are tabulated in Table 1. Noticeably, increasing the damage level to 5 dpa produces a mixture of small spherical bubbles and large faceted bubbles in NT Ag as shown in Fig. 3(c). Comparing with spherical bubbles, the large faceted bubbles carry much lower He pressure and He-to-vacancy ratio. Such pressure release may result from various bubble growth and coarsening mechanism, such as loop punching and bubble migration and coalescence, upon which the stress field surrounding the bubbles will change in concurrent with the volume increment [8]. The change in stress field may lead to different dislocation barrier strength of bubbles, which we will discuss in the following sections.

In addition to the formation of bubbles, SFT is another common type of irradiation-induced defects in face-centered cubic (FCC) metals with low stacking fault energy [59–61]. However, previous studies suggested that He would promote cavity formation and suppress SFT formation [62]. This argument is further supported by Wang et al. in their study of He irradiation damage on Cu/Ag multilayers, where SFTs were only observed in the region without He atoms [13]. Furthermore, the high concentration of implanted He in NT Ag traps vacancies to form bubbles or He-vacancy complex. In this study, we observed few SFTs in the very shallow surface region with low He concentration (Fig. S4), and did not detect other SFTs as the He density increases with increasing ion penetration depth.

4.2. Strengthening mechanism in as-deposited NT Ag

It has been reported that under uniaxial compression normal to the twin planes, the dominant deformation mechanism of NT metals is dislocation pile-up and dislocation transmission across

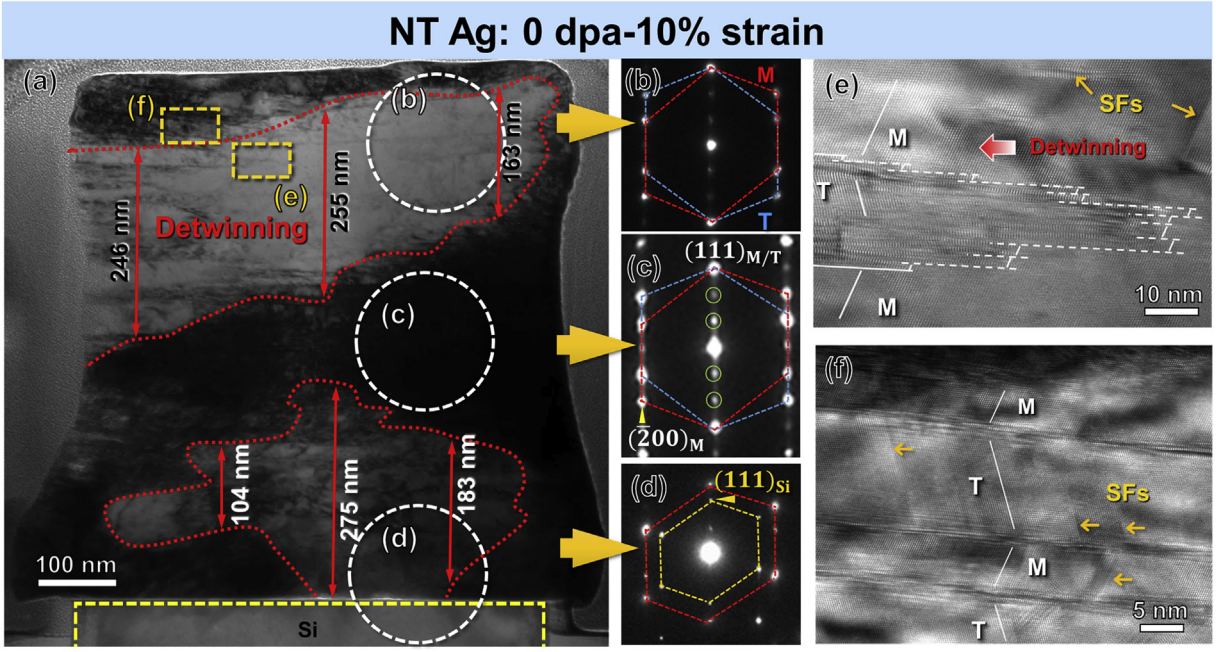

Fig. 9. TEM images of the as-deposited NT Ag pillar after compression. (a) XTEM micrograph showing the overview of the deformed pillar. (b–d) SAD patterns taken from the top, middle and bottom portion revealing the evolution of twin structures. The detwinning regions near the top and bottom center are outlined by dotted lines. (e) HRTEM micrograph taken from box e in (a) showing the detwinning process. The white dash lines trace the sharp migration steps of ITBs, which are three {111} atomic layers high. (f) SFs inclined with CTBs were observed after deformation, indicating dislocation-TB interactions.

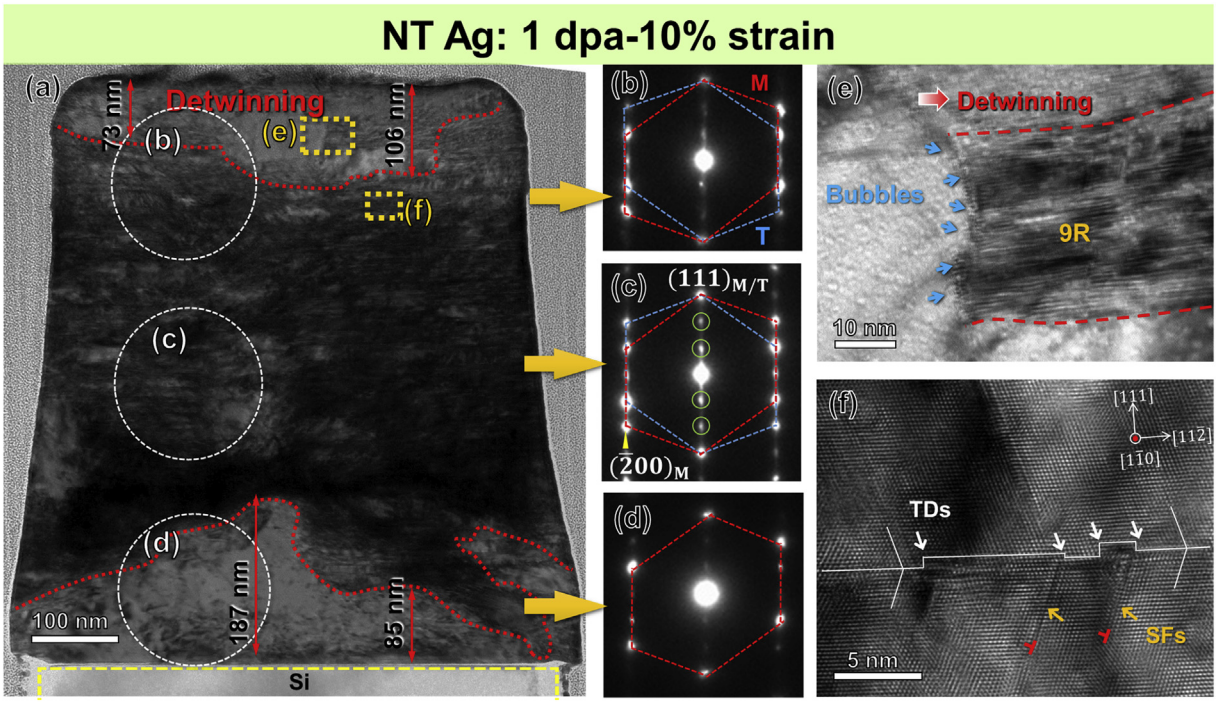

Fig. 10. TEM micrographs of the deformed pillar of NT Ag irradiated to 1 dpa to a strain level of 10%. (a) Low-magnification XTEM micrograph showing the overview of a deformed pillar. (c–d) SAD taken from the top, middle and bottom portion revealing the evolution of twin structures. The detwinning region near the top and bottom center are outlined by dotted lines. (e) HRTEM taken from box e showing the detwinning process. (f) Interaction of glide partials with CTBs leads to formation of multiple twinning dislocations (TDs).

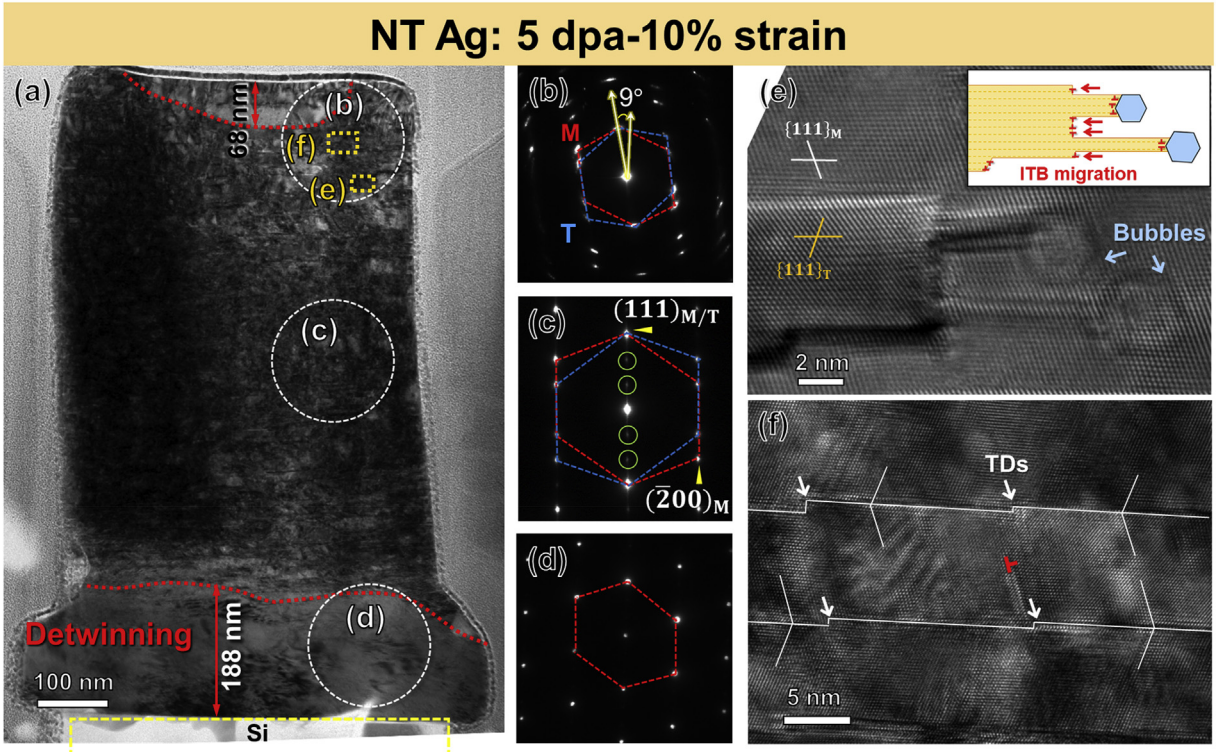

Fig. 11. TEM micrographs of the deformed pillar of NT Ag irradiated to 5 dpa. (a) Low-magnification XTEM micrograph showing the overview of deformed pillar. (c–d) SAD taken from the top, middle and bottom portion revealing the evolution of twin structures. The detwinning region near the top and bottom center are outlined by dotted lines. (e) HRTEM taken from box e shows that part of ITBs are pinned by bubbles. The inset is the schematic illustration of the pinning process. (f) TDs formed after deformation as evidenced by the jerky steps along CTBs.

TBs [63,64]. Due to the slip discontinuity across TBs, gliding dislocations must interact with TBs in order to continue their motion once impinged upon TBs. This transmission process is evident from our post-compression TEM analysis of deformed pristine NT Ag pillar, which shows numerous dislocation debris terminating at CTBs as shown in Fig. 9(f).

The strengthening mechanism of NT Ag is governed by dislocation pile-up and can be described by Hall-Petch relationship as suggested by previous study [65]. If we assume CTBs as strong as multilayer interface in blocking dislocations, the critical resolved shear stress for dislocation transmission can be expressed as [65]:

$$\tau_{HP} = \tau_0 + \left(\frac{Gb\tau^*}{(1-\nu)\pi h'}\right)^{1/2} \quad (5)$$

where τ_0 is the critical shear stress to initiate dislocation gliding, G is the shear modulus, b is the magnitude of burgers vector, τ^* is the barrier strength of interface, ν is passion radio, and h' is the average distance between obstacles. τ^* can be estimated by [65]:

$$\tau^* = \left(\frac{k_{HP}^2 \pi(1-\nu)}{Gb}\right) \quad (6)$$

where k_{HP} is the slope of the Hall-Petch plot. According to Bufford et al., the τ^* is calculated to be 0.532 GPa. By assuming Taylor factor is 3.06, i.e. $\sigma_{flow} \approx 3\tau^*$, the upper limit of flow stress of NT Ag is estimated to be 1.60 GPa [65]. The stress-strain curve in Fig. 5(k) showed that the ultimate compressive stress (UCS) of pristine NT Ag (black curve) is ~820 MPa, which is ~50% of the estimated maximum strength.

4.3. Irradiation induced hardening

Irradiation induced hardening is tightly associated with the interactions between dislocations and irradiation induced defects, such as dislocation loops, SFTs, voids and He bubbles [5]. Dislocation loops were considered as strong obstacles for dislocation motion, while He bubbles were generally considered as weak barriers and their barrier strength would increase with increasing He/vacancy ratio [66]. The Friedel-Kroupa-Hirsch (FKH) model is widely used to approximate the increase of yield strength due to He bubbles [66]:

$$\Delta\sigma_B = \frac{1}{8} M\mu b d_B N_B^{2/3} \quad (7)$$

Where $\Delta\sigma_B$ is the increment of yield stress, $\frac{1}{8}$ is the FKH factor given the inherent barrier strength of He bubbles [67,68], M is the Taylor factor, which is typically 3.06 for FCC metals, μ is the shear modulus, b is the magnitude of Burgers vector which is 0.286 nm for Ag,. The calculation yields a strength increment of 76.0 MPa for CG Ag and 49.3 MPa for NT Ag after irradiation to 1 dpa. For NT Ag irradiated to 5 dpa, the hardening due to small spherical bubbles is estimated to be 31 MPa while large faceted bubbles contribute to strength increment by 43 MPa.

The dispersed barrier model is developed to estimate the irradiation hardening due to dislocation loops:

$$\Delta\sigma_D = M\alpha'\mu b\sqrt{d_D N_D} \quad (8)$$

where α' is the average barrier strength of irradiation induced defect and is taken as 0.2 for the calculation [5], d_D is the average loop size, and N_D is the average loop density. Previous studies suggest that in irradiated materials with multiple types of defects, the estimation of total hardening depends on both the obstacle strength and the relative concentrations of these defects. Especially, when composing of obstacles that have more dissimilar barrier strength, the amount of radiation hardening can be better estimated using the linear summation. For He irradiated Ag, the majority of defects are He bubbles (weak obstacles) and dislocation loops (strong obstacles). Therefore, the superposition is used to estimate the total amount hardening due to radiation induced defects:

$$\Delta\sigma_{total} = \sum_i \Delta\sigma_i = \Delta\sigma_B + \Delta\sigma_D \quad (9)$$

where $\Delta\sigma_B$ is the amount of hardening due to He bubbles, and $\Delta\sigma_D$ is the strength increment due to dislocation loops. The calculation result for CG Ag and NT Ag after irradiation is tabulated in Table 2.

As shown in Table 2, the hardening calculated using classic models are insufficient to account for the measured strength increment in NT Ag after 1 dpa and 5 dpa irradiation. The disparity may result from the underestimation of bubble density as bubbles overlap with each other and affect the accurate measurement. The large quantity of He atoms outside the He bubbles could also contribute to the extra hardening. Previous simulation study shows that interstitial He atoms in the vicinity of dislocation can readily migrate to the dislocation core and are strongly trapped by the dislocation with a binding energy exceeding 2 eV, thus retarding the dislocation movement [69]. High concentration of He interstitials were reported to result in hardening especially when approaching a critical He concentration of ~1 at% or a damage level of ~1 dpa [8,70]. However, the quantitative description of the hardening due to He within the lattice can be difficult considering that He can exist in a variety locations (twin boundaries and grain interior) and their concentration is hard to determine. Furthermore, previous studies suggest that the barrier strength of bubbles are highly dependent on bubble pressure and He-to-vacancy ratio [71,72]. Comparing NT Ag irradiated to 1 dpa with 5 dpa, the hardening is even more drastic in 1 dpa irradiation, which is a bit surprising. In the NT Ag irradiated to 5 dpa, a large portion of He resides in the large faceted bubbles. The hexagon morphology and large radius imply lower bubble pressure and stress field as we discussed earlier, which could weaken the pinning effect of these large bubbles on dislocation motion when comparing with small spherical bubbles in the 1 dpa irradiated NT Ag.

An additional strengthening mechanism for NT Ag may come from the extra stress required for dislocation transmission across “thickened” TBs. As shown in Fig. S3, TBs become defective with thick SFs ribbons formed adjacent to the CTBs after irradiation. MD simulation studies on He irradiated NT Cu revealed that SFs decorated along CTBs could strengthen the TBs by making the dislocation transmission (across TBs) more difficult [73]. It is suggested that SFs will facilitate the cross-slip of screw dislocations onto CTBs instead of transmitting across the CTBs. For mixed dislocations, partial dislocations constrict before entering CTBs and the constriction increases the energy barrier for slip transfer [73]. Furthermore, a recent study on the mechanical properties of FCC Co found that SF ribbons can block mobile dislocations and induce prominent strengthening and work hardening [74].

4.4. Deformation induced detwinning

Fig. 9(e) shows the slanted TBs with diffused 9Rs in deformed as-deposited NT Ag pillar, suggesting that twin lamellae underwent detwinning driven by Shockley partial migration. Frequent detwinning was observed in as-deposited NT Ag after irradiation. In comparison, moderate detwinning was found in the NT Ag

Table 2
Summary of size and density of He bubbles and dislocation loops as well as strengthening in CG Ag and NT Ag after irradiation.

		Bubbles			Defect clusters			Strength increment	
		d_B (nm)	N_B($\times 10^{24}$ m^{-3})	$\Delta\sigma_B$ (MPa)	d_D (nm)	N_D($\times 10^{24}$ m^{-3})	$\Delta\sigma_D$ (MPa)	Calculated $\Delta\sigma$ (MPa)	Experimental $\Delta\sigma$ (MPa)
CG Ag_1 dpa		1.6 ± 0.3	2.1 ± 0.2	86	2.8±0.6	0.12±0.02	96	182	169
NT Ag_1 dpa		1.2 ± 0.3	1.4 ± 0.2	49	2.6±0.5	0.11±0.01	89	138	291
NT Ag	Spherical	1.5 ± 0.4	0.5 ± 0.1	31	3.7±1.0	0.12±0.01	111	185	216
5 dpa	Faceted	3.8 ± 0.7	0.2 ± 0.2	43					

irradiated to 1 dpa and 5 dpa. As shown in Figs. 9(a), 10(a) and 11(a), the detwinning region is confined to the top, ~106 and 68 nm deep in irradiated Ag, much smaller than that in the as-deposited Ag (~255 nm).

Irradiation induced He bubbles may play important role in curtailing the detwinning process. According to recent experiments and MD simulation studies, irradiation induced defects can increase the possibility of cross slip in both body-centered cubic (BCC) and FCC metal pillars, thus create cross-links and superjogs and act as sources for dislocation generation [75,76]. Using in-situ mechanical tests on He implanted Cu pillar, Ding et al. revealed that a large amount of partial dislocations were emitted from the He bubble surface [77]. It is likely that the high-density He bubbles in NT Ag may retard the collective glide of partials and thus alleviate detwinning; and emit dislocations to interact with gliding partials and hence disturb their further migration. As seen from Figs. 9(e) and 10(e), ITBs from the deformed region in as-deposited Ag become diffused with long “tails”, while the ones in irradiated Ag are generally “truncated” with bubbles decorating around 9R phase. For the large faceted bubbles generated in the NT Ag irradiated to 5 dpa, their interactions with ITBs result in the bubble-drag effect on ITB motion, which effectively retard the migration of ITBs as evidenced in Fig. 11(e). Further investigations will be conducted to study the influence of He bubble size, pressure and He-to-vacancy on the pinning effect of bubbles on ITB migrations.

5. Conclusion

The microstructure evolution and mechanical behaviors of He ion irradiated NT Ag (1 and 5 dpa) were investigated. Irradiation generated high-density He bubbles and induced thick SF ribbons along CTBs. Moderate increase of twin spacing was observed. Irradiation to 5 dpa produced a mixture of small spherical bubbles and large hexagonal bubbles. In-situ micropillar compression tests reveal a more prominent strength increment in NT Ag irradiated to 1 dpa than 5 dpa, implying the barrier strength of bubbles could vary as a function of bubble pressure and He-to-vacancy ratio. Meanwhile, SFs generated during irradiation may further strengthen the TBs by blocking dislocation transmission across TBs. Post-compression TEM analysis of the deformed pillars revealed the important role of He bubbles in curtailing detwinning in irradiated NT Ag.

Data availability statement

The data that support the findings of this study are available from the corresponding author upon reasonable request.

CRediT authorship contribution statement

T. Niu: Conceptualization, Investigation, Methodology, Writing - original draft. **Jin Li:** Conceptualization, Investigation, Methodology. **Y. Zhang:** Investigation, Formal analysis. **J. Cho:** Investigation, Validation. **Jie Ding:** Investigation. **R. Su:** Investigation, Formal analysis. **S. Xue:** Investigation, Data curation. **C. Fan:** Investigation. **Z. Shang:** Validation, Investigation. **Di Chen:** Resources. **Y. Wang:** Resources. **H. Wang:** Supervision, Project administration. **X. Zhang:** Conceptualization, Methodology, Writing - review & editing, Supervision, Funding acquisition.

Declaration of competing interest

The authors declare that they have no known competing financial interests or personal relationships that could have appeared to influence the work reported in this paper.

Acknowledgements

We acknowledge financial support by NSF-CMMI-MOM 1728419. H. Wang acknowledges the support from the U.S. Office of Naval Research (N00014-16-1-2778). Helium ion beam irradiation was performed at the Center for Integrated Nanotechnologies (CINT), an Office of Science User Facility operated for the U.S. Department of Energy (DOE) Office of Science. Los Alamos National Laboratory, an affirmative action equal opportunity employer, is managed by Triad National Security, LLC for the U.S. Department of Energy’s NNSA, under contract 89233218CNA000001. Materials Science Microscopy Center at Purdue University is also acknowledged.

Appendix A. Supplementary data

Supplementary data to this article can be found online at https://doi.org/10.1016/j.jnucmat.2020.152392.

References

[1] M. Griffiths, A review of microstructure evolution in zirconium alloys during irradiation, J. Nucl. Mater. 159 (1988) 190–218.
[2] R. Schäublin, Z. Yao, N. Baluc, M. Victoria, Irradiation-induced stacking fault tetrahedra in fcc metals, Phil. Mag. 85 (2005) 769–777.
[3] S.J. Zinkle, K. Farrell, Void swelling and defect cluster formation in reactor-irradiated copper, J. Nucl. Mater. 168 (1989) 262–267.
[4] B.N. Singh, On the influence of grain boundaries on void growth, Phil. Mag.: J. Theor. Exp. Appl. Phys. 28 (1973) 1409–1413.
[5] G.S. Was, Fundamentals of Radiation Materials Science: Metals and Alloys, springer, 2016.
[6] S.J. Zinkle, G.S. Was, Materials challenges in nuclear energy, Acta Mater. 61 (2013) 735–758.
[7] N. Hashimoto, T.S. Byun, K. Farrell, S.J. Zinkle, Deformation microstructure of neutron-irradiated pure polycrystalline metals, J. Nucl. Mater. 329–333 (2004) 947–952.
[8] H. Trinkaus, B.N. Singh, Helium accumulation in metals during irradiation – where do we stand? J. Nucl. Mater. 323 (2003) 229–242.
[9] K.Y. Yu, Y. Liu, C. Sun, H. Wang, L. Shao, E.G. Fu, X. Zhang, Radiation damage in helium ion irradiated nanocrystalline Fe, J. Nucl. Mater. 425 (2012) 140–146.
[10] X.-M. Bai, A.F. Voter, R.G. Hoagland, M. Nastasi, B.P. Uberuaga, Efficient annealing of radiation damage near grain boundaries via interstitial emission, Science 327 (2010) 1631–1634.
[11] C. Sun, K.Y. Yu, J.H. Lee, Y. Liu, H. Wang, L. Shao, S.A. Maloy, K.T. Hartwig, X. Zhang, Enhanced radiation tolerance of ultrafine grained Fe–Cr–Ni alloy, J. Nucl. Mater. 420 (2012) 235–240.

[12] C. Sun, M. Song, K.Y. Yu, Y. Chen, M. Kirk, M. Li, H. Wang, X. Zhang, In situ evidence of defect cluster Absorption by grain boundaries in Kr ion irradiated nanocrystalline Ni, Metall. Mater. Trans. 44 (2013) 1966–1974.
[13] M. Wang, I.J. Beyerlein, J. Zhang, W.-Z. Han, Defect-interface interactions in irradiated Cu/Ag nanocomposites, Acta Mater. 160 (2018) 211–223.
[14] N. Li, M. Nastasi, A. Misra, Defect structures and hardening mechanisms in high dose helium ion implanted Cu and Cu/Nb multilayer thin films, Int. J. Plast. 32–33 (2012) 1–16.
[15] N. Li, J.J. Carter, A. Misra, L. Shao, H. Wang, X. Zhang, The influence of interfaces on the formation of bubbles in He-ion-irradiated Cu/Mo nanolayers, Phil. Mag. Lett. 91 (2011) 18–28.
[16] E.G. Fu, A. Misra, H. Wang, L. Shao, X. Zhang, Interface enabled defects reduction in helium ion irradiated Cu/V nanolayers, J. Nucl. Mater. 407 (2010) 178–188.
[17] N. Li, E.G. Fu, H. Wang, J.J. Carter, L. Shao, S.A. Maloy, A. Misra, X. Zhang, He ion irradiation damage in Fe/W nanolayer films, J. Nucl. Mater. 389 (2009) 233–238.
[18] K.Y. Yu, D. Bufford, C. Sun, Y. Liu, H. Wang, M.A. Kirk, M. Li, X. Zhang, Removal of stacking-fault tetrahedra by twin boundaries in nanotwinned metals, Nat. Commun. 4 (2013) 1377.
[19] Y. Chen, J. Li, K.Y. Yu, H. Wang, M.A. Kirk, M. Li, X. Zhang, In situ studies on radiation tolerance of nanotwinned Cu, Acta Mater. 111 (2016) 148–156.
[20] J. Li, Y. Chen, H. Wang, X. Zhang, In situ studies on twin-thickness-dependent distribution of defect clusters in heavy ion-irradiated nanotwinned Ag, Metall. Mater. Trans. 48 (2017) 1466–1473.
[21] Y. Chen, K.Y. Yu, Y. Liu, S. Shao, H. Wang, M.A. Kirk, J. Wang, X. Zhang, Damage-tolerant nanotwinned metals with nanovoids under radiation environments, Nat. Commun. 6 (2015) 7036.
[22] J. Li, K.Y. Yu, Y. Chen, M. Song, H. Wang, M.A. Kirk, M. Li, X. Zhang, In situ study of defect migration kinetics and self-healing of twin boundaries in heavy ion irradiated nanotwinned metals, Nano Lett. 15 (2015) 2922–2927.
[23] I.J. Beyerlein, A. Caro, M.J. Demkowicz, N.A. Mara, A. Misra, B.P. Uberuaga, Radiation damage tolerant nanomaterials, Mater. Today 16 (2013) 443–449.
[24] X. Zhang, K. Hattar, Y. Chen, L. Shao, J. Li, C. Sun, K. Yu, N. Li, M.L. Taheri, H. Wang, J. Wang, M. Nastasi, Radiation damage in nanostructured materials, Prog. Mater. Sci. 96 (2018) 217–321.
[25] O. El-Atwani, K. Hattar, J.A. Hinks, G. Greaves, S.S. Harilal, A. Hassanein, Helium bubble formation in ultrafine and nanocrystalline tungsten under different extreme conditions, J. Nucl. Mater. 458 (2015) 216–223.
[26] G.M. Cheng, W.Z. Xu, Y.Q. Wang, A. Misra, Y.T. Zhu, Grain size effect on radiation tolerance of nanocrystalline Mo, Scripta Mater. 123 (2016) 90–94.
[27] C. Du, S. Jin, Y. Fang, J. Li, S. Hu, T. Yang, Y. Zhang, J. Huang, G. Sha, Y. Wang, Z. Shang, X. Zhang, B. Sun, S. Xin, T. Shen, Ultrastrong nanocrystalline steel with exceptional thermal stability and radiation tolerance, Nat. Commun. 9 (2018) 5389.
[28] O. El-Atwani, J.A. Hinks, G. Greaves, J.P. Allain, S.A. Maloy, Grain size threshold for enhanced irradiation resistance in nanocrystalline and ultrafine tungsten, Mater. Res. Lett. 5 (2017) 343–349.
[29] O. El-Atwani, K. Hattar, J.A. Hinks, G. Greaves, S.S. Harilal, A. Hassanein, Helium bubble formation in ultrafine and nanocrystalline tungsten under different extreme conditions, J. Nucl. Mater. 458 (2015) 216–223.
[30] Q.M. Wei, N. Li, N. Mara, M. Nastasi, A. Misra, Suppression of irradiation hardening in nanoscale V/Ag multilayers, Acta Mater. 59 (2011) 6331–6340.
[31] K.Y. Yu, Y. Liu, E.G. Fu, Y.Q. Wang, M.T. Myers, H. Wang, L. Shao, X. Zhang, Comparisons of radiation damage in He ion and proton irradiated immiscible Ag/Ni nanolayers, J. Nucl. Mater. 440 (2013) 310–318.
[32] Y.F. Zhang, Q. Li, S.C. Xue, J. Ding, D.Y. Xie, J. Li, T. Niu, H. Wang, H. Wang, J. Wang, X. Zhang, Ultra-strong nanotwinned Al-Ni solid solution alloys with significant plasticity, Nanoscale 10 (2018) 22025–22034.
[33] S. Xue, Q. Li, D.Y. Xie, Y.F. Zhang, H. Wang, H. Wang, J. Wang, X. Zhang, High strength, deformable nanotwinned Al–Co alloys, Mater. Res. Lett. 7 (2019) 33–39.
[34] Q. Li, S. Xue, J. Wang, S. Shao, A.H. Kwong, A. Giwa, Z. Fan, Y. Liu, Z. Qi, J. Ding, H. Wang, J.R. Greer, H. Wang, X. Zhang, High-strength nanotwinned Al alloys with 9R phase, Adv. Mater. 30 (2018) 1704629.
[35] X. Zhang, A. Misra, H. Wang, T.D. Shen, M. Nastasi, T.E. Mitchell, J.P. Hirth, R.G. Hoagland, J.D. Embury, Enhanced hardening in Cu/330 stainless steel multilayers by nanoscale twinning, Acta Mater. 52 (2004) 995–1002.
[36] I.J. Beyerlein, X. Zhang, A. Misra, Growth twins and deformation twins in metals, Annu. Rev. Mater. Res. 44 (2014) 329–363.
[37] Y.M. Wang, F. Sansoz, T. LaGrange, R.T. Ott, J. Marian, T.W. Barbee Jr., A. V Hamza, Defective twin boundaries in nanotwinned metals, Nat. Mater. 12 (2013) 697.
[38] W.Z. Han, M.J. Demkowicz, E.G. Fu, Y.Q. Wang, A. Misra, Effect of grain boundary character on sink efficiency, Acta Mater. 60 (2012) 6341–6351.
[39] M.J. Demkowicz, O. Anderoglu, X. Zhang, A. Misra, The influence of $\sum 3$ twin boundaries on the formation of radiation-induced defect clusters in nanotwinned Cu, J. Mater. Res. 26 (2011) 1666–1675.
[40] M. Niewczas, R.G. Hoagland, Molecular dynamic studies of the interaction of a/6⟨112⟩ Shockley dislocations with stacking fault tetrahedra in copper. Part II: intersection of stacking fault tetrahedra by moving twin boundaries, Phil. Mag. 89 (2009) 727–746.
[41] Y. Liu, N. Li, D. Bufford, J.H. Lee, J. Wang, H. Wang, X. Zhang, In situ nanoindentation studies on detwinning and work hardening in nanotwinned monolithic metals, J. Occup. Med. 68 (2016) 127–135.
[42] K.Y. Yu, D. Bufford, F. Khatkhatay, H. Wang, M.A. Kirk, X. Zhang, In situ studies of irradiation-induced twin boundary migration in nanotwinned Ag, Scripta Mater. 69 (2013) 385–388.
[43] J. Wang, N. Li, O. Anderoglu, X. Zhang, A. Misra, J.Y. Huang, J.P. Hirth, Detwinning mechanisms for growth twins in face-centered cubic metals, Acta Mater. 58 (2010) 2262–2270.
[44] C. Fan, J. Li, Z. Fan, H. Wang, X. Zhang, In situ studies on the irradiation-induced twin boundary-defect interactions in Cu, Metall. Mater. Trans. 48 (2017) 5172–5180.
[45] N. Li, J. Wang, J.Y. Huang, A. Misra, X. Zhang, Influence of slip transmission on the migration of incoherent twin boundaries in epitaxial nanotwinned Cu, Scripta Mater. 64 (2011) 149–152.
[46] J. Wang, R.G. Hoagland, A. Misra, Room-temperature dislocation climb in metallic interfaces, Appl. Phys. Lett. 94 (2009) 131910.
[47] L. Zhang, Y. Shibuta, C. Lu, X. Huang, Interaction between nano-voids and migrating grain boundary by molecular dynamics simulation, Acta Mater. 173 (2019) 206–224.
[48] D.B. Williams, C.B. Carter, in: D.B. Williams, C.B. Carter (Eds.), The Transmission Electron Microscope BT - Transmission Electron Microscopy: A Textbook for Materials Science, Springer US, Boston, MA, 1996, pp. 3–17.
[49] H. Trinkaus, Energetics and formation kinetics of helium bubbles in metals, Radiat. Eff. 78 (1983) 189–211.
[50] W. Kesternich, Helium trapping at dislocations, precipitates and grain boundaries, Radiat. Eff. 78 (1983) 261–273.
[51] G.E. Lucas, The evolution of mechanical property change in irradiated austenitic stainless steels, J. Nucl. Mater. 206 (1993) 287–305.
52 S.J. Zinkle, 1.03-Radiation-Induced effects on microstructure, Compr. Nucl. Mater. 1 (2012) 65–98.
53 R.E. Stoller, 1.11-primary radiation damage formation, Compr. Nucl. Mater. (2012) 293–332.
[54] Q. Wei, N. Li, K. Sun, L.M. Wang, The shape of bubbles in He-implanted Cu and Au, Scripta Mater. 63 (2010) 430–433.
[55] P.J. Goodhew, The Shape of an Overpressurized Bubble, 1981.
[56] Q.M. Wei, Y.Q. Wang, M. Nastasi, A. Misra, Nucleation and growth of bubbles in He ion-implanted V/Ag multilayers, Phil. Mag. 91 (2011) 553–573.
[57] A. Polian, M. Grimsditch, Elastic properties and density of helium up to 20 {GPa), Europhys. Lett. 2 (1986) 849–855.
[58] L. Vitos, A. V Ruban, H.L. Skriver, J. Kollár, The surface energy of metals, Surf. Sci. 411 (1998) 186–202.
[59] D.J. Bacon, F. Gao, Y.N. Osetsky, The primary damage state in fcc, bcc and hcp metals as seen in molecular dynamics simulations, J. Nucl. Mater. 276 (2000) 1–12.
[60] * R.S, Z. Yao, N. Baluc, M. Victoria, Irradiation-induced stacking fault tetrahedra in fcc metals, Phil. Mag. 85 (2005) 769–777.
[61] J. Li, C. Fan, Q. Li, H. Wang, X. Zhang, In situ studies on irradiation resistance of nanoporous Au through temperature-jump tests, Acta Mater. 143 (2018) 30–42.
[62] I. Mukouda, Y. Shimomura, T. Iiyama, Y. Harada, Y. Katano, T. Nakazawa, D. Yamaki, K. Noda, Microstructure in pure copper irradiated by simultaneous multi-ion beam of hydrogen, helium and self ions, J. Nucl. Mater. 283–287 (2000) 302–305.
[63] D. Jang, X. Li, H. Gao, J.R. Greer, Deformation mechanisms in nanotwinned metal nanopillars, Nat. Nanotechnol. 7 (2012) 594, https://doi.org/10.1038/nnano.2012.116.
[64] T. Zhu, H. Gao, Plastic deformation mechanism in nanotwinned metals: an insight from molecular dynamics and mechanistic modeling, Scripta Mater. 66 (2012) 843–848.
[65] D. Bufford, H. Wang, X. Zhang, High strength, epitaxial nanotwinned Ag films, Acta Mater. 59 (2011) 93–101.
[66] S.J. Zinkle, Y. Matsukawa, Observation and analysis of defect cluster production and interactions with dislocations, J. Nucl. Mater. 329–333 (2004) 88–96.
[67] J. Friedel, R. Smoluchowski, N. Kurti, Dislocations: International Series of Monographs on Solid State Physics, Elsevier Science, 2013.
[68] F. Kroupa, P.B. Hirsch, Elastic interaction between prismatic dislocation loops and straight dislocations, Discuss. Faraday Soc. 38 (1964) 49–55.
[69] H.L. Heinisch, F. Gao, R.J. Kurtz, E.A. Le, Interaction of helium atoms with edge dislocations in α-Fe, J. Nucl. Mater. 351 (2006) 141–148.
[70] H. Trinkaus, The effect of cascade induced gas resolution on bubble formation in metals, J. Nucl. Mater. 318 (2003) 234–240.
[71] L. Yang, X.T. Zu, F. Gao, S.M. Peng, H.L. Heinisch, X.G. Long, R.J. Kurtz, Dynamic interactions of helium-vacancy clusters with edge dislocations in α-Fe, Phys. B Condens. Matter 405 (2010) 1754–1758.
[72] R. Schäublin, Y.L. Chiu, Effect of helium on irradiation-induced hardening of iron: a simulation point of view, J. Nucl. Mater. 362 (2007) 152–160.
[73] C. Fan, Q. Li, J. Ding, Y. Liang, Z. Shang, J. Li, R. Su, J. Cho, D. Chen, Y. Wang, J. Wang, H. Wang, X. Zhang, Helium irradiation induced ultra-high strength nanotwinned Cu with nanovoids, Acta Mater. 177 (2019) 107–120.
[74] R. Su, D. Neffati, S. Xue, Q. Li, Z. Fan, Y. Liu, H. Wang, Y. Kulkarni, X. Zhang, Deformation mechanisms in FCC Co dominated by high-density stacking faults, Mater. Sci. Eng., A 736 (2018) 12–21.
[75] J.S. Robach, I.M. Robertson, B.D. Wirth, A. Arsenlis, In-situ transmission electron microscopy observations and molecular dynamics simulations of dislocation-defect interactions in ion-irradiated copper, Phil. Mag. 83 (2003) 955–967.
[76] J.Y. Zhang, F.L. Zeng, K. Wu, Y.Q. Wang, X.Q. Liang, G. Liu, G.J. Zhang, J. Sun,

Size-dependent plastic deformation characteristics in He-irradiated nanostructured Cu/Mo multilayers: competition between dislocation-boundary and dislocation-bubble interactions, Mater. Sci. Eng., A 673 (2016) 530–540.

[77] M.-S. Ding, J.-P. Du, L. Wan, S. Ogata, L. Tian, E. Ma, W.-Z. Han, J. Li, Z.-W. Shan, Radiation-induced helium nanobubbles enhance ductility in submicron-sized single-crystalline copper, Nano Lett. 16 (2016) 4118–4124.